



UNIVERSITY OF LEEDS

This is a repository copy of *Extraction of 3D quantitative maps using EDS-STEM tomography and HAADF-EDS bimodal tomography*.

White Rose Research Online URL for this paper:
<https://eprints.whiterose.ac.uk/167739/>

Version: Accepted Version

Article:

Yuan, Y, MacArthur, KE, Collins, SM orcid.org/0000-0002-5151-6360 et al. (4 more authors) (2020) Extraction of 3D quantitative maps using EDS-STEM tomography and HAADF-EDS bimodal tomography. *Ultramicroscopy*. 113166. ISSN 0304-3991

<https://doi.org/10.1016/j.ultramic.2020.113166>

© 2020, Elsevier. This manuscript version is made available under the CC-BY-NC-ND 4.0 license <http://creativecommons.org/licenses/by-nc-nd/4.0/>.

Reuse

This article is distributed under the terms of the Creative Commons Attribution-NonCommercial-NoDerivs (CC BY-NC-ND) licence. This licence only allows you to download this work and share it with others as long as you credit the authors, but you can't change the article in any way or use it commercially. More information and the full terms of the licence here: <https://creativecommons.org/licenses/>

Takedown

If you consider content in White Rose Research Online to be in breach of UK law, please notify us by emailing eprints@whiterose.ac.uk including the URL of the record and the reason for the withdrawal request.



eprints@whiterose.ac.uk
<https://eprints.whiterose.ac.uk/>

Extraction of 3D quantitative maps using EDS-STEM tomography and HAADF-EDS bimodal tomography

Yu Yuan^a, Katherine E. MacArthur^b, Sean M. Collins^c, Nicolas Brodusch^a, Frédéric Voisard^a, Rafal E. Dunin-Borkowski^b, Raynald Gauvin^a

^a Department of Mining and Materials Engineering, McGill University, 3610 Rue University, Montreal, Québec, Canada, H3A 0C5

^b Ernst Ruska-Centre for Microscopy and Spectroscopy with Electrons (ER-C-1), Wilhelm-Johnen Str., 52425 Jülich, Germany

^c School of Chemical and Process Engineering & School of Chemistry, University of Leeds, Leeds, LS2 9JT, United Kingdom

E-mail address: yu.yuan@mail.mcgill.ca (Yu Yuan), k.macarthur@fz-juelich.de (Katherine E. MacArthur), s.m.collins@leeds.ac.uk (Sean M. Collins), nicolas.brodusch@mcgill.ca (Nicolas Brodusch), frederic.voisard@mail.mcgill.ca (Frédéric Voisard), r.dunin-borkowski@fz-juelich.de (Rafal E. Dunin-Borkowski), raynald.gauvin@mcgill.ca (Raynald Gauvin).

Corresponding Author:

Raynald Gauvin

Department of Mining and Materials Engineering

McGill University

M.H. Wong Building

3610 Rue University

Montreal, QC, Canada

H3A 0C5

Tel: (514) 398-8951

Fax: (514) 398-4492

Abstract

Electron tomography has been widely applied to three-dimensional (3D) morphology characterization and chemical analysis at the nanoscale. A HAADF-EDS bimodal tomographic (HEBT) reconstruction technique has been developed to extract high resolution element-specific information. However, the reconstructed elemental maps cannot be directly converted to quantitative compositional information. In this work, we propose a quantification approach for obtaining elemental weight fraction maps from the HEBT reconstruction technique using the physical parameters extracted from a Monte Carlo code, MC X-ray. A similar quantification approach is proposed for the EDS-STEM tomographic reconstruction. The performance of the two quantitative reconstruction methods, using the simultaneous iterative reconstruction technique, are evaluated and compared for a simulated dataset of a two-dimensional phantom sample. The effects of the reconstruction parameters including the number of iterations and the weight of the HAADF signal are discussed. Finally, the two approaches are applied to an experimental dataset to show the 3D structure and quantitative elemental maps of a particle of flux melted metal-organic framework glass.

Key words: EDS-STEM tomography, HAADF-EDS bimodal tomography, electron-induced X-ray quantification, three-dimensional elemental map.

1. Introduction

Electron tomography is a technique that characterizes the three-dimensional (3D) structure of a typically nanoscale object from a tilt series of two-dimensional (2D) projections [1] and has been widely used in biological science [2, 3] and materials science [4]. Different image modes are available for electron tomography. The scanning transmission electron microscope (STEM) high-angle annular dark-field (HAADF) image is typically used for most cases in the field of material science to minimize the diffraction contrast that dominates in low-angle scattering which is the case for conventional bright-field (BF) or dark-field (DF) images of crystalline materials [5]. The intensity of the HAADF-STEM signal is strongly dependent on the atomic number and the projected thickness. HAADF tomography is thus sensitive to 3D chemical composition information. One disadvantage of HAADF tomography is that it only contains the accumulated information of all elements, which means the structures with different compositions but similar average atomic numbers cannot be distinguished. On the other hand, energy dispersive

spectroscopy (EDS) STEM tomography can be used to extract element-specific distribution maps, and it has been applied to a wide range of materials including bimetallic nanoparticles [6], metallurgical samples [7], and semiconductor nanowires [8]. However, in comparison to HAADF-STEM tomography, it has poor signal-to-noise ratio (SNR) because of low count rates associated with the low probability of X-ray emission and the poor signal collection efficiency of available X-ray detectors [9, 10].

HAADF/ADF-STEM images have been used in EDS-STEM tomography for object contour determination [11], absorption correction [12], and shadowing effect correction [13]. Zhong et al. [14] proposed an HAADF-EDS bimodal tomographic (HEBT) reconstruction technique that uses HAADF-STEM and EDS-STEM simultaneously to extract 3D elemental maps. The technique links the HAADF image and EDS maps through response ratio factors using a linear relationship, i.e., the HAADF image is a weighted summation of the EDS maps of different elements. Using this technique, the element-specific features of EDS maps are extracted while also preserving the high SNR of the HAADF image. It has been successfully applied to the characterization of a nanowire device [15]. Nevertheless, it is not straightforward to obtain quantitative compositional information from the reconstructed intensities. To obtain the 3D elemental weight/atomic fraction maps, a quantification method needs to be applied.

There are currently three approaches to the quantification of EDS-STEM images: the Cliff-Lorimer method [16], the ζ -factor method [17], and the partial cross-section method [10]. The Cliff-Lorimer method connects the weight fractions, C_A and C_B , of two constituent elements A and B to their detected characteristic X-ray intensities, I_A and I_B using the following equation [16]:

$$\frac{C_A}{C_B} = k_{AB} \frac{I_A}{I_B}, \quad (1)$$

where k_{AB} is the Cliff-Lorimer factor (k -factor), which can be estimated using theoretical calculations or experiments [17]. The theoretical calculation of k -factors is fast but gives rise to relatively high systematic errors ($\pm 10\% - 20\%$ for the quantification of 2D elemental map) [17, 18], while the experimental determination is accurate with relative errors around $\pm 1\%$ but is often complicated and time-consuming [17]. An improved quantitative approach, the ζ -factor method, gives the relationship between the detected X-ray intensity of element A , I_A and the mass thickness ρt (ρ and t are the specimen density and thickness) as follows [17]:

$$\rho t = \zeta_A \frac{I_A}{C_A D_e}, \quad (2)$$

where ζ_A is the ζ -factor and D_e is the total electron dose. The ζ -factor method shows great advantages in absorption correction, spatial resolution calculation, etc. because it refines the thickness information. Moreover, the experimental determination of the ζ -factor is easier as it can be performed using single element standards.

A further, recently emerging approach uses EDS partial cross-sections to quantify X-ray counts in an absolute manner [10, 19]. The EDS partial cross-section of a single atom of element A is determined from a pure element standard using the following equation:

$$\sigma_{par}^A = \frac{I_A}{D_e n_A t}, \quad (3)$$

where $n_A t$ is the atom density per unit area in atoms/m², in which n_A is the atom volume density and t is the thickness. Although this approach is based on the ζ -factor method, the implementation of this approach is simpler because it is on an absolute scale [19]. A similar quantification method to the ζ -factor method and partial cross-section is used in our calculation, although here the correction factor is determined through physical models instead of experiments.

The main objective of this paper is to present a quantification method using theoretical cross-sections to obtain 3D elemental maps from both EDS-STEM tomography and HEBT through the simultaneous iterative reconstruction technique (SIRT). The effects of the reconstruction parameters are also studied in this work. Using a 2D phantom sample, the image qualities of the direct reconstructed maps and the quantified maps are investigated and compared for EDS-STEM tomography and HEBT. Both techniques are then applied to an experimental dataset of a particle of flux melted metal-organic framework glass, denoted $a_g [(ZIF-67)_{0.2}(ZIF-62)_{0.8}]$, where a_g refers to amorphous glass structure, ZIF-67 and ZIF-62 refer to two compositionally distinct zeolitic imidazolate frameworks, and the subscripts refer to the relative fraction in the bulk glass. The synthesis and traditional quantitative EDS tomography of the glass particle have been explicitly described in previous reports [20, 21]. Here we look specifically at the implementation and results from the quantified HEBT reconstruction.

2. Methods

The following calculations are based on the thin film approximation, which means that the absorption and secondary fluorescence are negligible, as is the multiple scattering of the incident electrons. The quantifications of the EDS-STEM tomographic and HEBT reconstructions and the simulation of the HAADF and EDS signals using MC X-ray [22] will be introduced in this section.

2.1. Quantification of the EDS-STEM tomographic reconstruction

The measured characteristic intensity of a certain X-ray line of element A from a thin film is expressed using the equation [23]:

$$I_A = N_V \frac{\sigma_{ion}^A \omega_A p_A}{M_A} C_A \rho t D_e \left(\frac{\Omega}{4\pi} \right) \varepsilon_A, \quad (4)$$

where N_V is Avogadro's number, σ_{ion}^A is the ionization cross-section, ω_A is the fluorescence yield, p_A is the relative intensity, M_A is the atomic weight, Ω is the detector solid angle, and ε_A is the detector efficiency. To better demonstrate the relationship between the X-ray intensity and the weight fraction, equation 4 can be written as follows:

$$I_A = n f_A C_A \rho t, \quad (5)$$

where n is a constant for a certain measurement and f_A is an element-specific factor, which are calculated as follows:

$$n = N_V D_e \left(\frac{\Omega}{4\pi} \right), \quad (6)$$

$$f_A = \frac{\sigma_{ion}^A \omega_A p_A \varepsilon_A}{M_A}. \quad (7)$$

In electron tomography, for a heterogeneous sample, the measured characteristic X-ray intensity for a single measurement of the projection image can be expressed in an integral form along the electron trajectory inside the sample, t' ,

$$I_A = n f_A \int C_A(t') \rho(t') d(t'). \quad (8)$$

The continuous line integral can be replaced by a discrete ray-sum [14]:

$$I_A = nf_A \sum_{j=1}^N w_j C_{A,j} \rho_j, \quad (9)$$

where w_j is determined by the volume intersected between the electron beam and the j^{th} voxel [24]. N is the number of voxels in the specimen for the reconstruction.

For EDS-STEM tomography, multiple measurements are performed for various beam positions and tilt angles. The number of measurements, M equals the product of the number of tilt angles and the number of beam positions. For a certain element A , the X-ray intensity for the i^{th} measurement, $I_{A,i}$ can be expressed as follows:

$$I_{A,i} = nf_A \sum_{j=1}^N w_{ij} C_{A,j} \rho_j. \quad (10)$$

The tomography reconstruction is often formulated as a least square minimization:

$$\mathbf{X}_A^* = \underset{\mathbf{X}_A}{\operatorname{argmin}} \|\mathbf{I}_A - \mathbf{W}\mathbf{X}_A\|_2^2, \quad (11)$$

where $\mathbf{I}_A \in \mathbf{R}^M$ is the X-ray intensity matrix, $\mathbf{W} \in \mathbf{R}^{M \times N}$ is the projection matrix, and $\mathbf{X}_A \in \mathbf{R}^N$ is the reconstruction quantity. According to equation 10, we know that the reconstructed quantity for the j^{th} voxel, $\mathbf{X}_{A,j} = nf_A C_{A,j} \rho_j$. Since the sum of the weight fractions of the constituent elements for a certain voxel is always one, i.e., $\sum_{A=1}^k C_{A,j} = 1$, where k is the number of elements, using a similar calculation to the ζ -factor method, considering that the solid angle is the same for all the elements, we have

$$C_{A,j} = \frac{\mathbf{X}_{A,j}/f_A}{\sum_{A=1}^k \mathbf{X}_{A,j}/f_A}. \quad (12)$$

According to the definitions, the partial cross-section can be calculated using the factor f_A by $\sigma_{par}^A = f_A \cdot \Omega/4\pi \cdot M_A$.

SIRT is used to solve the least square problem [25]. SIRT updates the reconstructed values at each iteration using the data from all the projections simultaneously [26]. Its primary advantage is a reduced sensitivity to noise or other errors in under-sampled experimental data [27]. Unfortunately, it has the semi-convergence property, that the error initially decreases but starts to increase after some iterations when dealing with noisy data [28]. In this work, a non-negativity

constraint was applied to SIRT algorithm by setting individual negative voxels to zero in each iteration since the reconstructed values should always remain non-negative [29].

The normalization in equation 12 may magnify the noise of the reconstructed map by changing a small value to one. Therefore, prior to this normalization, a thresholding was performed in order to define the voxels within the particle, that any intensities smaller than the threshold were set to zero based on the summation of all the elemental maps of $\mathbf{X}_{A,j}/f_A$. The exact threshold value was determined using a modified edge spread function (ESF) fitting approach [21]. The approach calculates the particle volume for a series of threshold values, and the variation of the threshold relative to the particle volume can be fitted using the ESF. Therefore, the smallest gradient of the particle volume over the threshold corresponds to the most appropriate threshold value. The same process was applied to the quantification of the HEBT reconstruction. For both the EDS-STEM and HEBT reconstruction, the thresholding step was applied after the reconstruction process as a post-processing step for the purpose of visualizing and interpreting the quantification within the volume of the particle.

2.2. Quantification of the HEBT reconstruction

It is worth noticing that HEBT can be applied only when two conditions are satisfied: first, both the HAADF and EDS data fulfill the projection requirement, that the signal is a monotonic function of the thickness and composition [30], and secondly, the HAADF signals are the weighted sum of the EDS signals for all the elements present [31].

The HAADF-STEM signal I^H is the number of electrons that are scattered at high angles and can be expressed as the sum of the scattered electrons by each element present in the specimen [14]:

$$I^H = D_e^H N_v \sum_{A=1}^k \sigma_{ela}^A \frac{\int C_A(t') \rho(t') d(t')}{M_A}, \quad (13)$$

where D_e^H is the electron dose for HAADF measurement, A is the index of the constituent element, k is the number of elements in the specimen, σ_{ela}^A is the elastic scattering cross-section, and $C_A(t')$ is the weight fraction of element A at t' . It can be written in the same form as equation 9:

$$I^H = D_e^H N_v \sum_{A=1}^k z_A \sum_{j=1}^N w_{ij} C_{A,j} \rho_j, \quad (14)$$

where $z_A = \sigma_{ela}^A / M_A$.

The HEBT reconstruction technique proposed by Zhong et al. [14] links the HAADF signals with the EDS signals using a response ratio factor r_A :

$$I^H = \sum_{A=1}^k r_A I_A \quad (15)$$

and,

$$r_A = \frac{D_e^H N_v z_A}{n f_A} \quad (16)$$

Since the value of r_A might differ for various instruments or experimental setups, it is typically estimated using the measured intensities I^H and I_A through linear regression. The reconstruction using HEBT is to minimize the least square of the measured and estimated signals (see [14] for more details),

$$\mathbf{X}^{b*} = \underset{\mathbf{X}^b}{\operatorname{argmin}} \|\mathbf{I}^b - \mathbf{W}^b \mathbf{X}^b\|_2^2 \quad (17)$$

$$\text{where } \mathbf{I}^b = \begin{pmatrix} (1-\alpha)r_1 \mathbf{I}_1 \\ \vdots \\ (1-\alpha)r_A \mathbf{I}_e \\ \vdots \\ (1-\alpha)r_k \mathbf{I}_k \\ \alpha \mathbf{I}^H \end{pmatrix}, \mathbf{W}^b = \begin{pmatrix} (1-\alpha)\mathbf{W} & \dots & \emptyset & \dots & \emptyset \\ \vdots & \dots & \vdots & \dots & \vdots \\ \emptyset & \dots & (1-\alpha)\mathbf{W} & \dots & \emptyset \\ \vdots & \dots & \vdots & \dots & \vdots \\ \emptyset & \dots & \emptyset & \dots & (1-\alpha)\mathbf{W} \\ \alpha\mathbf{W} & \dots & \alpha\mathbf{W} & \dots & \alpha\mathbf{W} \end{pmatrix},$$

and $\mathbf{X}^b = \begin{pmatrix} \mathbf{X}_1^b \\ \vdots \\ \mathbf{X}_A^b \\ \vdots \\ \mathbf{X}_k^b \end{pmatrix}$, where $\mathbf{X}_A^b \in \mathbf{R}^N$, in which $X_{A,j}^b = z_A C_{A,j} \rho_j$, and α is the balance factor between

the HAADF and EDS terms, which indicates the weight of the HAADF term ($0 < \alpha < 1$).

With the reconstructed quantity \mathbf{X}^b , the composition of element A for the j^{th} voxel can be calculated as follows:

$$C_{A,j} = \frac{X_{A,j}^b/z_A}{\sum_{A=1}^k X_{A,j}^b/z_A}. \quad (18)$$

2.3. Forward modeling using MC X-ray

The required physical parameters for the quantification including scattering and ionization cross-sections are extracted from MC X-ray [22], a Monte Carlo program for simulating electron trajectories within the solid and computing X-ray emissions. The physical models used for calculating those parameters are shown in Table 1. And the extracted physical parameters used in this work are listed in Table 2.

MC X-ray [22] was used to calculate the simulated HAADF and EDS signals from a phantom sample. The quantification processes using both EDS-STEM tomography and HEBT were applied to the simulated signals, and the reconstructed images (both before and after quantification) were compared with the phantom sample to assess the accuracy of each process. The HAADF detector inner collection angle used in MC X-ray for high angle and low angle are 611 and 94 mrad, respectively.

Table 1 Physical models used in MC X-ray [22]

Physical parameters	Physical models
Elastic scattering cross-section	Mott & Browning 1991 [32]
Ionization cross-section	Bote 2009 [33]
Fluorescence yield	Perkins et al. 1991 [34]
Relative intensity	Perkins et al. 1991 [34]

Table 2 Physical parameters extracted from MC X-ray

X-ray line	Ag L α	Au M α	Co K α	Zn K α
Incident beam energy (keV)	100		80	
Elastic scattering cross section (barn)	9.90×10^6	1.98×10^7	5.59×10^6	6.51×10^6
Ionization cross section (barn)	2.44×10^3	7.46×10^3	420	302

Fluorescence yield	0.057	0.030	0.369	0.466
Relative intensity	0.816	0.999	0.891	0.890

3. Results and discussion

3.1. A 2D phantom sample

3.1.1. Input

To assess the accuracy of the proposed quantification approaches, a 2D phantom sample of an alloyed Ag-Au nanoparticle, a slice on the X-Z plane, was created. The weight fractions of Ag and Au are presented in Figure 1. The phantom sample has a core-shell structure, in which the composition of the core is 80 wt% Au and 20 wt% Ag, while the shell has 20 wt% Au and 80 wt% Ag.

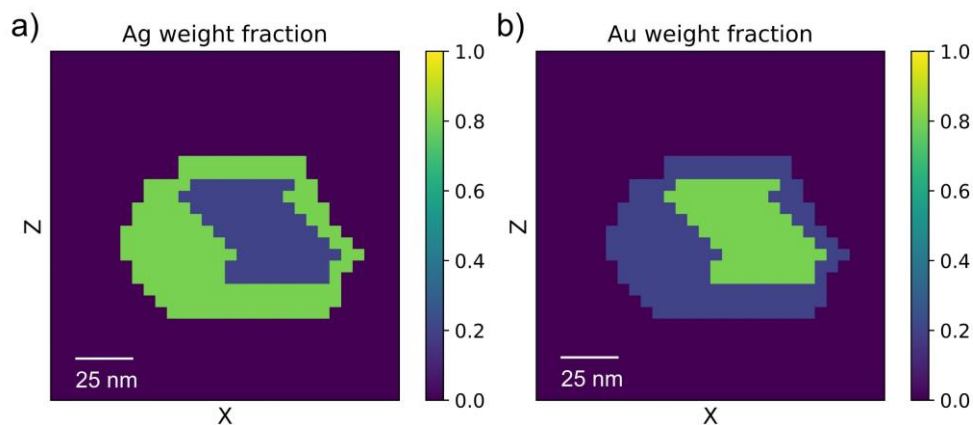


Figure 1 Weight fractions of a) Ag and b) Au for the phantom sample: a slice of Ag-Au alloyed particle with a core-shell structure. Core: 80 wt% Au and 20 wt% Ag; Shell: 20 wt% Au and 80 wt% Ag.

Simulations were performed using MC X-ray at 100 keV for 97 beam positions from -72 to 72 nm with a step size of 1.5 nm and 31 tilt angles from -75° to 75° with a step size of 5° . The HAADF sinogram (as presented in Figure 2 a) was obtained with a simulated electron number of 100,000 per pixel, which corresponds to an electron fluence of $444 \text{ e}/\text{A}^2$ (electrons per square angstrom). Pixels along the horizontal and vertical axes represent the signals for varying beam positions and varying tilt angles, respectively. To mimic reasonable experimental conditions, an acquisition time of 0.5 s for each pixel and a beam current of 100 pA were used, indicating an electron number of

3.121×10^8 per pixel, which corresponds to an electron fluence of 1.39×10^6 e/A². Since the experimental EDS signals follow a Poisson distribution [35], Poisson noise was applied to the simulated EDS sinograms, and the resulting sinograms of the Ag L α line and Au M α line are shown in Figure 2 b) and c), respectively.

Before performing the tomography reconstruction, a Gaussian filter with a standard derivation of 0.8 was applied to the EDS elemental maps as a denoise process to improve the SNR. It was implemented using the multidimensional Gaussian filter function in Python library SciPy [36]. The EDS sinograms with Gaussian filter are presented in Figure 2 d) and e). For both EDS-STEM tomography and HEBT, the EDS sinograms with Gaussian filter were used as input. And the original HAADF sinogram was used for HEBT.

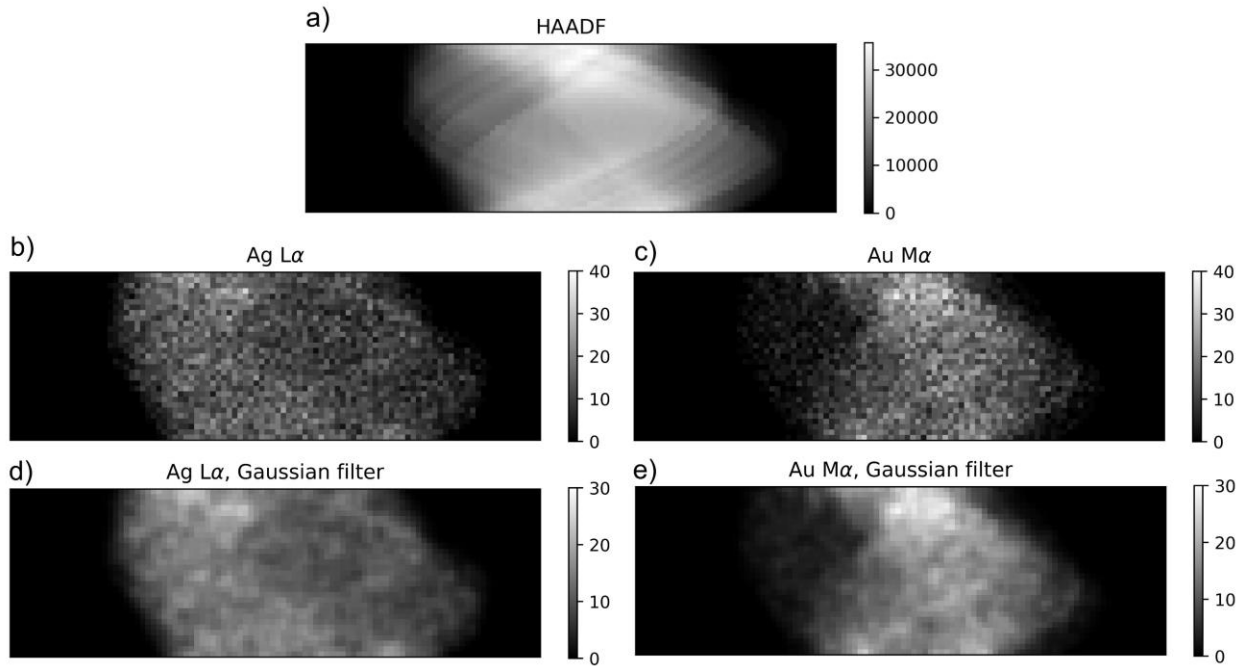


Figure 2 Sinograms of a) HAADF, b) EDS for the Ag L α line, c) EDS for the Au M α line, d) EDS for the Ag L α line adding a Gaussian filter, and e) EDS for the Au M α line adding a Gaussian filter. Pixels along the horizontal and vertical axes represent the signals for varying beam positions and varying tilt angles, respectively.

3.1.2. EDS-STEM tomographic reconstruction

The EDS-STEM tomographic reconstruction was first performed using SIRT for the sinograms shown in Figure 2 d) and e). The reconstructed images were computed for different numbers of iterations, $n = 20, 50$ and 100 , to investigate its effect. The reconstructed images of the quantity X_A for Ag and Au are presented in Figure 3. Note that the quantity X_A is not on an absolute scale.

For Ag after 20 iterations (as shown in Figure 3 a), the core-shell structure can be distinguished, in which the intensity of Ag is higher in the shell than the core. However, the boundaries both between the core and shell as well as between the object and background are blurry. When n increases to 50 (Figure 3 b), the contrast is improved, and the boundaries become clearer. At a higher n , however, an increased noise is observed (Figure 3 c) because of the over-fitting problem. As for Au, similarly, an increased noise is presented with an increase in n (as shown in Figure 3 d, e, and f). For all three numbers of iterations, the shape of the core with an increased Au intensity is well-preserved, while part of the boundaries is not correctly recognized. For example, several pixels in the bottom of the shell are recognized as background, which is due to the low SNR and large tilt angle increment (5° for this case) of the projection images and the relatively low concentration of Au in the shell.

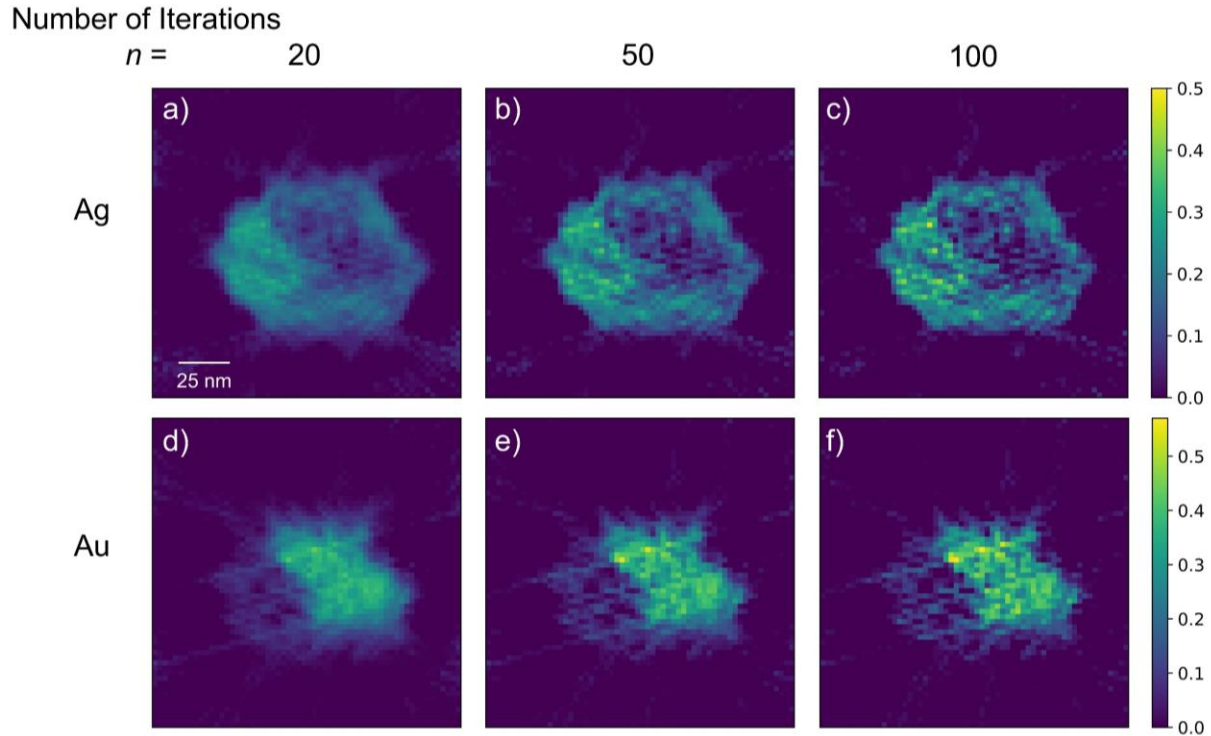


Figure 3 Ag and Au element maps reconstructed using SIRT through EDS-STEM tomography when the number of iterations $n = 20, 50,$ and 100 respectively. a), b), and c) are on the same intensity scale, and d), e), f) are on the same intensity scale.

To better assess the quality of the reconstructed image, two types of image quality metrics are calculated: structural similarity index (SSIM) and mean squared error (MSE). SSIM [37] evaluates the structural similarity between two images considering three components: luminance, contrast, and structure. Since the intensities of the reconstructed images are not on the same scale with the

reference image (phantom sample), only the structure component is compared. The structure component, s , of two signals \mathbf{x} and \mathbf{y} (with the same size) are calculated as follows [37]:

$$s(\mathbf{x}, \mathbf{y}) = \frac{\sigma_{xy} + C}{\sigma_x \sigma_y + C}, \quad (19)$$

where

$$\sigma_{xy} = \frac{1}{N-1} \sum_{i=1}^N (x_i - \mu_x)(y_i - \mu_y), \quad (20)$$

$$\sigma_x = \left(\frac{1}{N-1} \sum_{i=1}^N (x_i - \mu_x)^2 \right)^{1/2}, \quad (21)$$

$$\sigma_y = \left(\frac{1}{N-1} \sum_{i=1}^N (y_i - \mu_y)^2 \right)^{1/2}, \quad (22)$$

and C is a factor to avoid instability when $\sigma_x \sigma_y$ is very close to zero, N is the size of \mathbf{x} and \mathbf{y} , μ_x and μ_y are the average intensity of \mathbf{x} and \mathbf{y} . C is set to zero in our calculations but still included in equation 19 for consistency with common implementations. An SSIM value that is close to one means better structural similarity than for a value close to zero. MSE is the average of the squares of the errors between two signals. MSE between the direct reconstructed image \mathbf{X}_A and the reference image (Figure 1 a and b) is computed using a scaling factor since they are in different scales, and the scaling factor is chosen to minimize the MSE. For the quantified weight fraction maps, MSE is calculated directly without scaling.

Figure 4 shows the variations of a) SSIM and b) MSE relative to the number of iterations for the reconstructed images obtained using the EDS-STEM tomographic reconstruction. For both metrics, a better image quality for Au is found than for Ag. This difference is likely due to the slightly higher X-ray intensities of the Au $M\alpha$ line (as shown in Figure 2 d and e), which means lower noise from the sinogram. Alternatively, the higher contrast between the shell and the background for Ag than for Au may impair the image quality for Ag to a greater extent due to an imperfect boundary. As n increases, the image quality for Ag initially improves but then starts to fall off after 50 iterations, whilst for Au this drop off occurs after only 20 iterations. This is consistent with what we can observe qualitatively in Figure 3. Therefore, the approximately optimal value for the number of iterations for Ag and Au are 50 and 20, respectively.

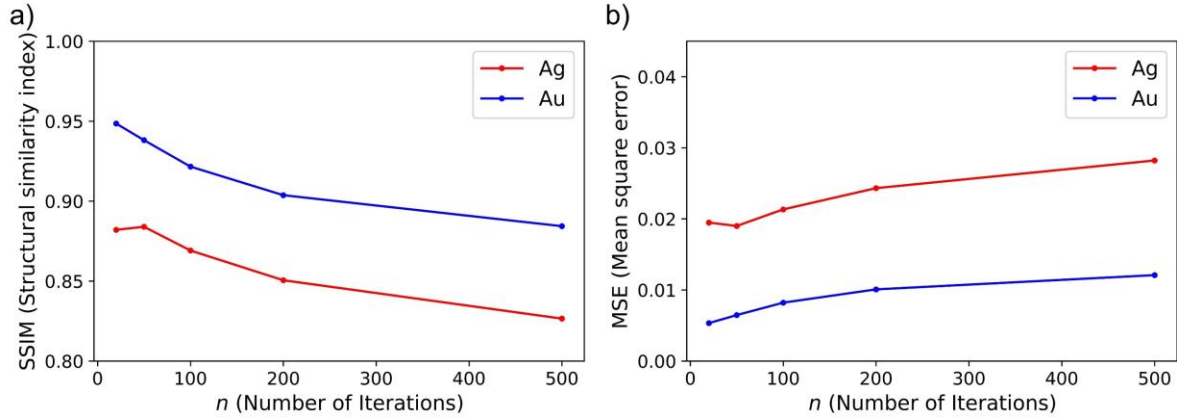


Figure 4 Variation of a) SSIM and b) MSE relative to n , the number of iterations for the EDS-STEM tomographic reconstruction.

From the reconstructed images of \mathbf{X}_A , Figure 3, the true weight fractions of Ag and Au were computed using equation 12. The computed weight fraction maps for different numbers of iterations are presented in Figure 5. In general, the core and shell are well segmented, and the compositions of both regions are close to the reference values. The boundary between the object and the background appears sharper after quantification primarily because the noise outside the object is removed by the thresholding step. The image quality of the quantitative element maps as shown in Figure 6 are thus slightly improved relative to the image quality of \mathbf{X}_A . The quantification process to a certain extent neutralizes the difference between the intensities of Ag and Au, making the relatively sharp boundary between the core and shell (as shown in Figure 3 a and d) become a ‘belt-like’ region (Figure 5 a and b) when the number of iterations is 20. The variation of the image quality relative to the number of iterations (Figure 6) presents a similar trend as that for the images of \mathbf{X}_A (Figure 4).

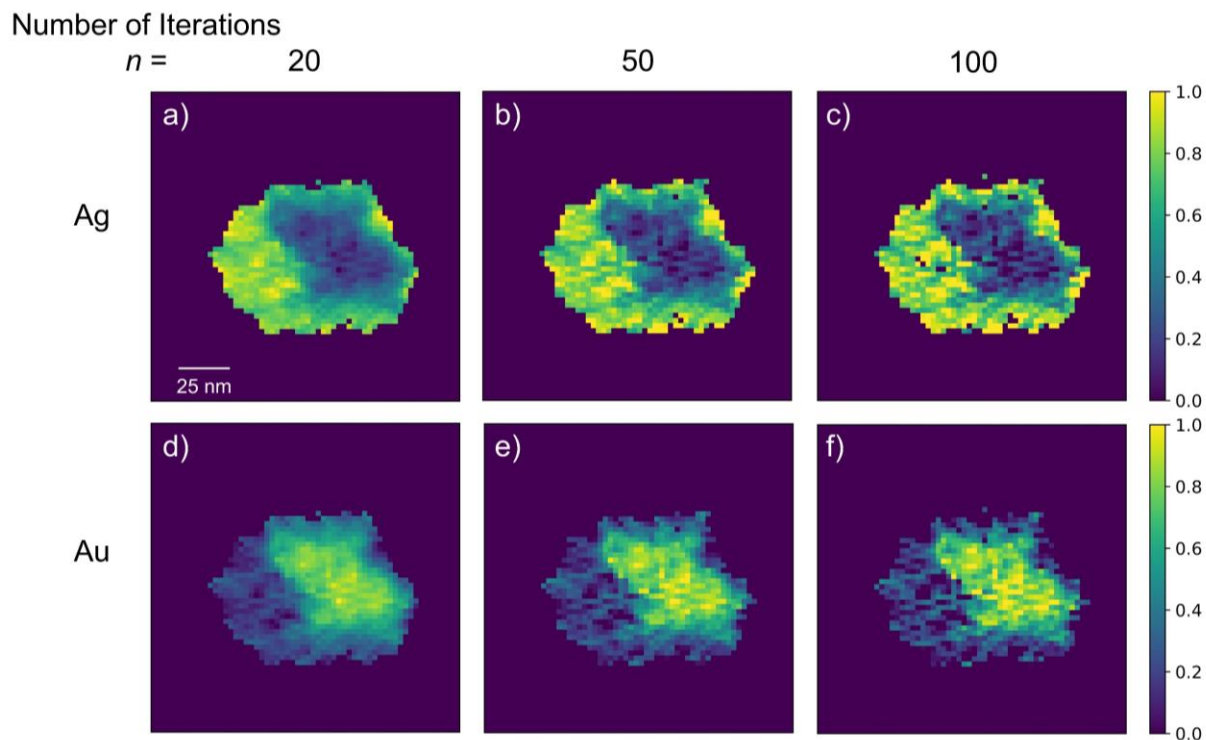


Figure 5 Quantitative elemental maps (weight fraction) of Ag and Au for different numbers of iterations, $n = 20, 50,$ and 100 . All figures are on the same intensity scale.

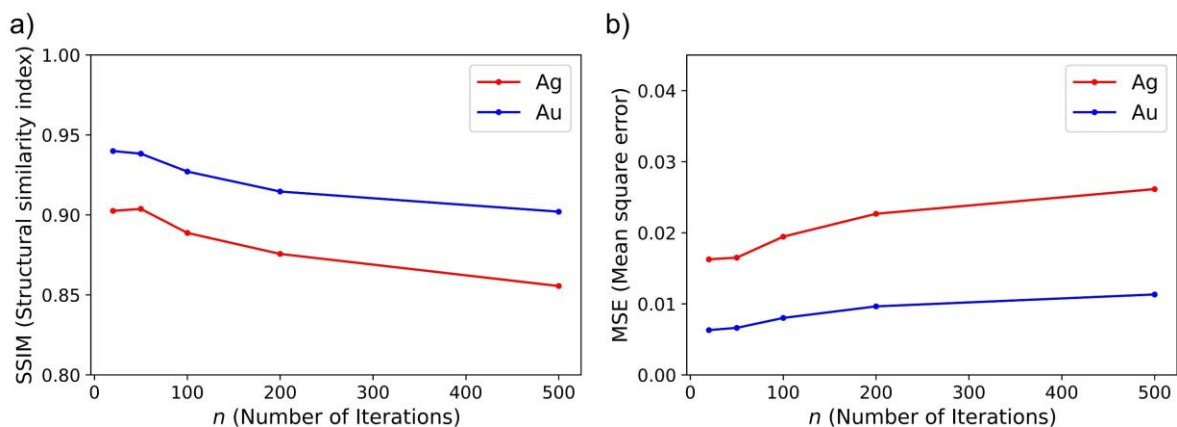


Figure 6 Variation of a) SSIM and b) MSE for the reconstructed weight fraction maps from EDS-STEM tomography as a function of n , the number of iterations.

3.1.3. HEBT reconstruction

In this section, results obtained using the HEBT reconstruction are presented. Figure 7 shows the reconstructed Z-contrast image from the HAADF-STEM sinogram after 50 iterations. Compared with the reconstructed elemental maps shown in the last section, the boundaries both between the object and background as well as between the core and shell can be distinguished

clearly, and there is notably higher contrast. It also shows an excellent agreement with the input phantom structure. Therefore, it is reasonable to assume the HEBT reconstruction has some advantages over the EDS-STEM tomographic reconstruction as it incorporates the HAADF signal.

The response ratio factors r_{Ag} and r_{Au} were calculated using the gradient descent method [38] to link the HAADF-STEM and EDS-STEM images by a linear relationship. The calculated r_{Ag} and r_{Au} are 805 and 987, respectively, with a coefficient of determination R^2 of 0.982, indicating that more than 98% of the measured data can be explained by the linear model.

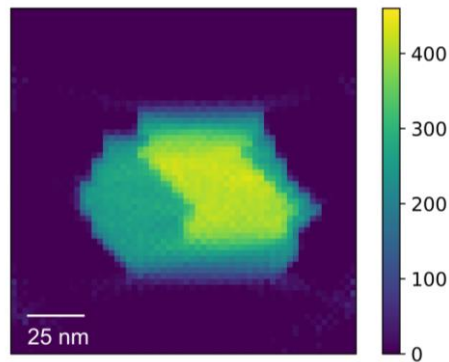


Figure 7 Reconstructed Z-contrast image from HAADF-STEM tomography after 50 iterations using SIRT.

Two parameters affect the HEBT reconstruction process: n , the number of iterations and α , the weight of the HAADF signal. We performed the HEBT reconstruction for different n : 100, 200, and 500, and varying α , ranging from 0 to 1. Note that the number of iterations required for the HEBT reconstruction is much larger than that for the EDS-STEM tomographic reconstruction due to the increased data volume. For the EDS-STEM tomographic reconstruction, the input data is the EDS sinogram for a certain X-ray line with a pixel size of M , while for the HEBT reconstruction, the input data is the EDS sinograms for all the X-ray lines of the elements present and the HAADF sinograms, with a total size of $M \times (k + 1)$, where k is the number of elements present in the specimen. Therefore, more data needs to be optimized for the HEBT reconstruction, requiring an increased number of iterations. Several numbers of iterations smaller than 100 were also tested, however they demonstrated far worse quality than the results presented here. The qualities of the reconstructed images for the quantity X^b are evaluated, taking Figure 1 as reference images.

The variations of SSIM and MSE are shown in Figure 8 a) and b), respectively, as a function of α for different n . A better image quality of Au is observed compared with Ag, which is similar to the results from EDS-STEM tomography. For each number of iterations, the image quality is first improved as α increases, and then deteriorates after reaching the best. To better investigate the effect of α , the weight of the HAADF signal, we present the reconstructed images for $\alpha = 0.7$, 0.8, and 0.9 after 200 iterations in Figure 9. As α changes from 0.7 to 0.8, the noise level appears suppressed since the low noise HAADF data dominates more. As it continues increasing to 0.9, though with less noise, the boundary between the shell and core becomes blurry, and the contrast deteriorates. Figure S1 presents the intensity profiles across the boundary for the elemental maps shown in Figure 9 to better observe the variation of the boundary with α . The variation is because as α increases, the EDS-STEM terms contribute less, which makes the optimization process to minimize the residuals of the EDS-STEM terms inefficient. If the residual of the HAADF-STEM term has been minimized while those for the EDS-STEM terms remain large, the back projection from the HAADF-STEM image will appear in the reconstructed elemental maps. Therefore, in this case, the reconstructed elemental maps of both Ag and Au become similar to the image from the HAADF-STEM reconstruction (Figure 7), showing worse contrast.

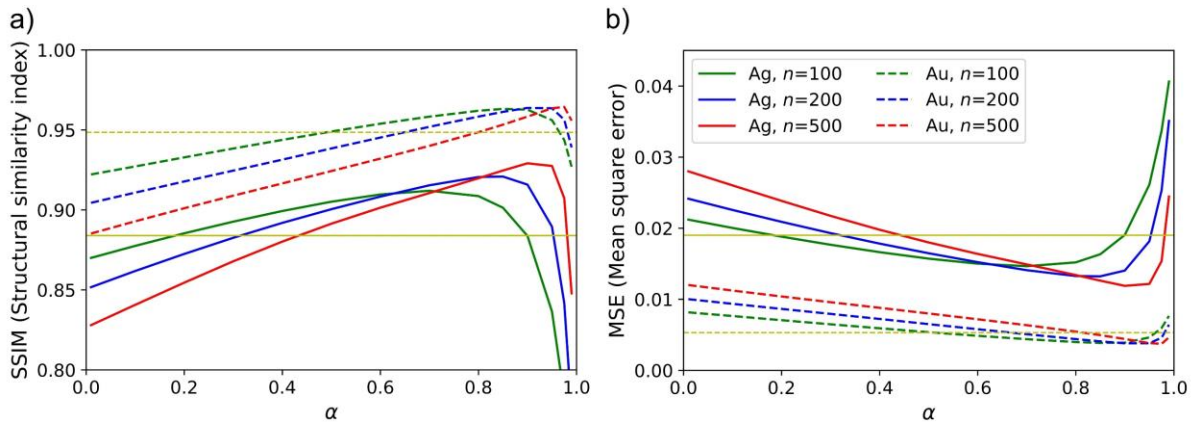


Figure 8 Variation of a) SSIM and b) MSE of Ag and Au as a function of α , the weight of the HAADF signal, for different n : 100 (green), 200 (blue), and 500 (red) for the direct reconstructed maps using HEBT. Solid lines represent the data for Ag, and dashed lines represent the data for Au. The yellow horizontal lines indicate the best image quality obtained using the EDS-STEM tomographic reconstruction.

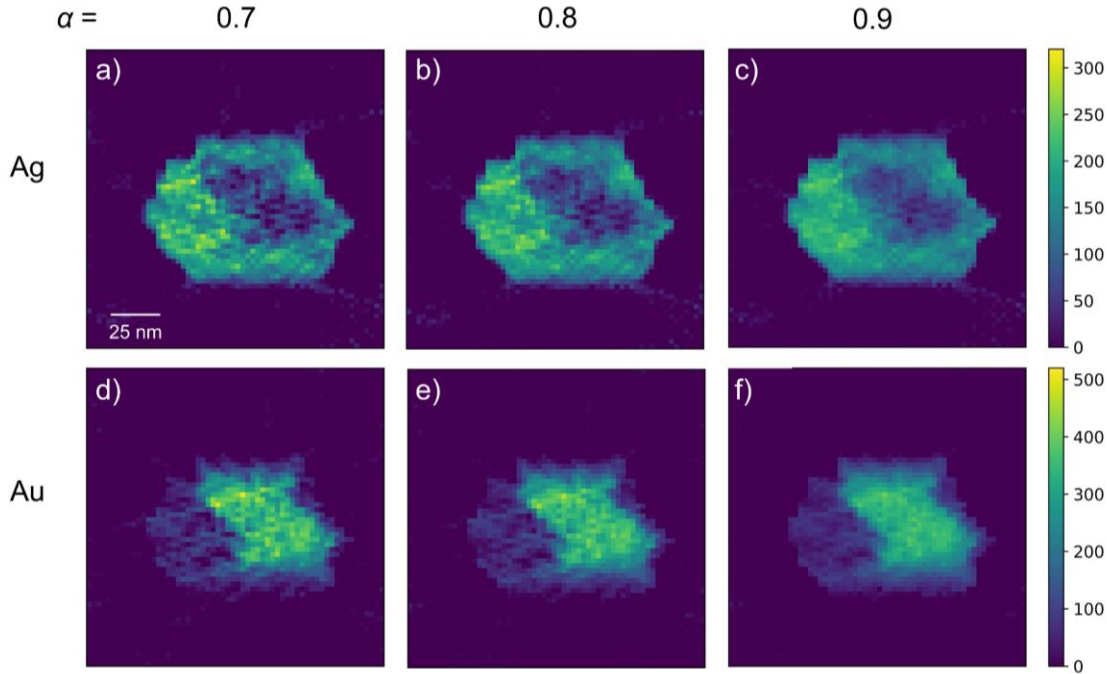


Figure 9 Elemental maps directly reconstructed using HEBT for Ag and Au for different α , the weight of the HAADF signal: 0.7, 0.8, 0.9 after 200 iterations. a), b), and c) are on the same intensity scale, and d), e), and f) are on the same intensity scale.

As n increases, the image quality typically improves before subsequently deteriorating due to the overfitting problem. Just as shown in Figure 10 d), e) and f), the Au elements map shows an improved contrast when n increases from 50 to 200. However, upon increasing to 500 iterations, the noise begins to dominate again. The approximately optimal value of n is thus found to be 200. Although, the optimal value of n changes as α increases. As shown in Figure 8, the approximately optimal value of n for Ag is 100 when α is smaller than 0.6, and the value changes to 200 when α is between 0.6 and 0.8. An optimal value around 500 is found for α larger than 0.8. This results from the inefficiency of the optimization process for the EDS-STEM terms as α increases. An increased number of iterations is required to reduce the appearance of the back projection of the HAADF-STEM image in the reconstructed elemental maps in the case when the residual of the HAADF-STEM term is minimized and those for the EDS-STEM terms remain large.

The yellow horizontal lines in Figure 8 represent the best reconstruction image quality obtained using the EDS-STEM tomographic reconstruction to be compared with the HEBT reconstruction. The best image quality is obtained when $n=50$ for Ag (yellow solid line) and 20 for Au (yellow dashed line). For both Ag and Au, the HEBT tomographic reconstruction shows better images under most circumstances as long as α is larger than 0.5. The element maps for Ag demonstrate a

greater improvement in image quality compared to Au possibly due to the fact that the image quality of Ag is more sensitive to the change in the boundary resulting from higher contrast between the shell and the background. When comparing the reconstructed images from EDS-STEM tomography (Figure 3) with that of HEBT (Figure 9 and Figure 10), one improvement that stands out is that the boundary between the object and the background is defined more clearly for HEBT (see Figure S2 for the comparison of the intensity profiles across the boundary). This is primarily a benefit of the high SNR of the HAADF sinogram. Within the object, the segmentation of the core and shell relies partly on the choice of the reconstruction parameters like n and α .

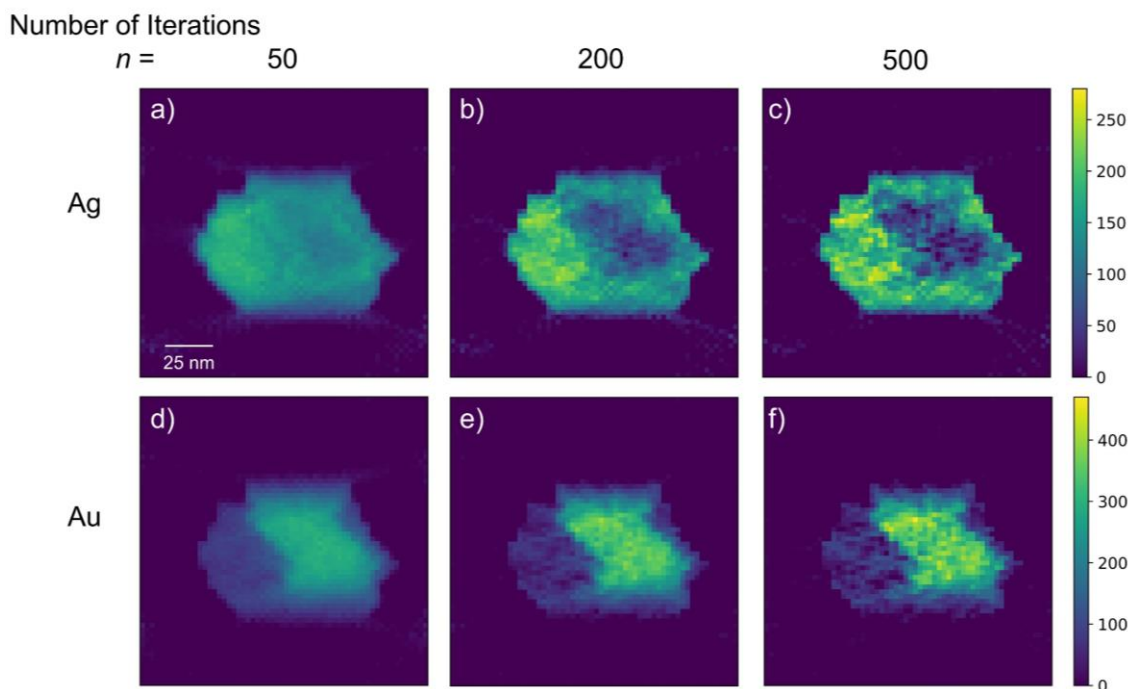


Figure 10 Elemental maps for Ag and Au directly reconstructed using HEBT for different n , the number of iterations: 50, 200, and 500 when $\alpha=0.9$ (α is the weight of the HAADF signal). a), b), c) are on the same intensity scale, and d), e), f) are on the same intensity scale.

From the reconstructed images of \mathbf{X}^b , the quantitative elemental maps of Ag and Au were calculated using equation 18. The quantitative elemental maps of Figure 9 and Figure 10 are shown in Figure 11 and Figure 12, respectively. Similar effects of n and α are observed as previously seen in the reconstructed images of \mathbf{X}^b . For the same number of iterations, an increase in α can reduce the level of noise but simultaneously results in a blurring of the boundary between the core and shell (see Figure S3 for the intensity profiles of the elemental maps shown in Figure 11). For a

constant α , an increase in n initially improves the contrast but subsequently brings more noise at higher α due to the over-fitting problem.

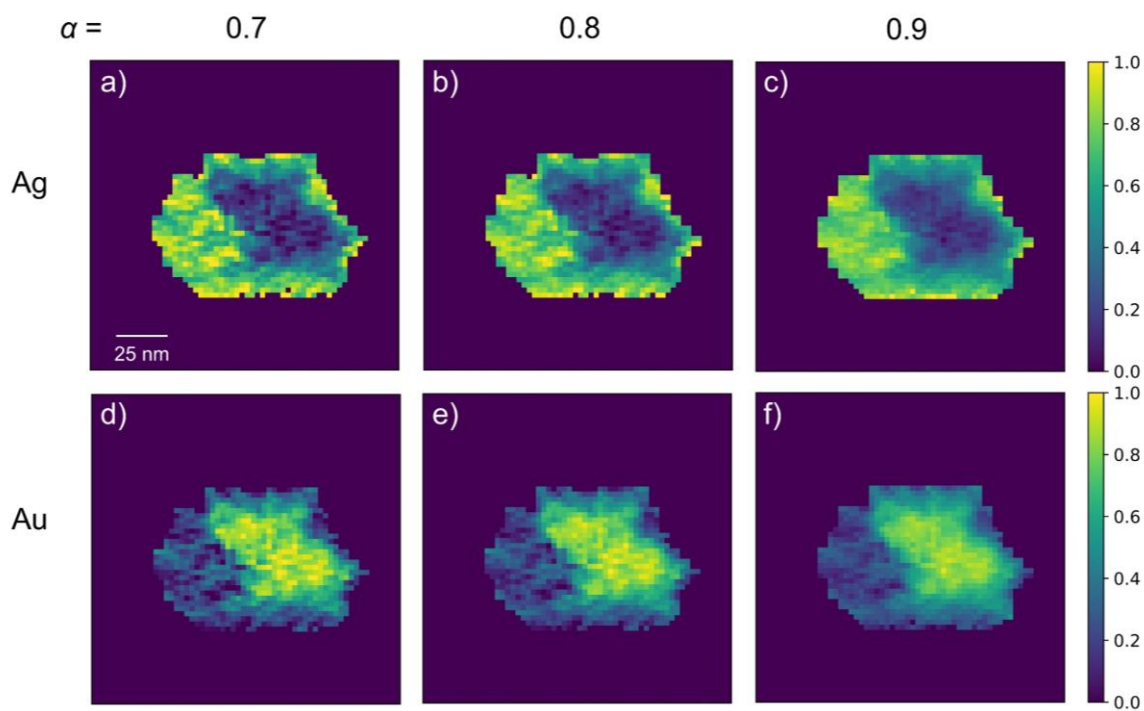


Figure 11 Quantitative elemental maps of Ag and Au (weight fraction) from HEBT for different α , the weight of the HAADF signal: 0.7, 0.8, 0.9 after 200 iterations. All figures are on the same intensity scale.

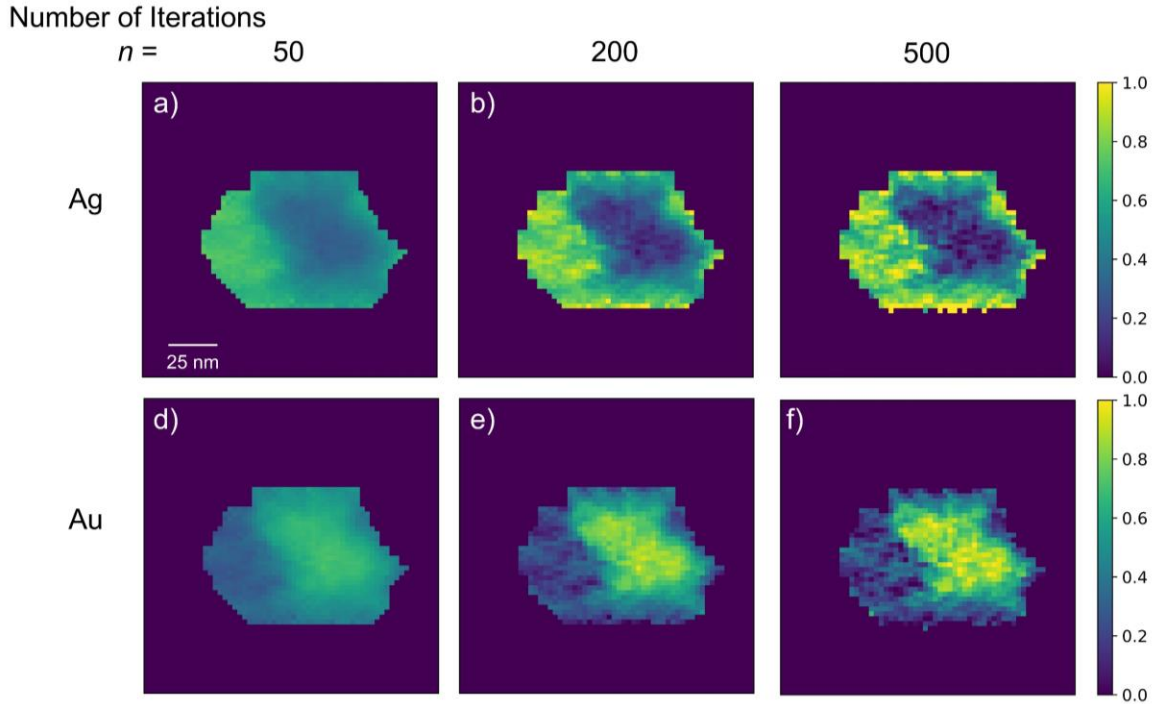


Figure 12 Quantitative elemental maps of Ag and Au (weight fraction) from HEBT for different n , the number of iterations: 50, 200, and 500 with $\alpha=0.9$ (α is the weight of the HAADF signal). All figures are on the same scale.

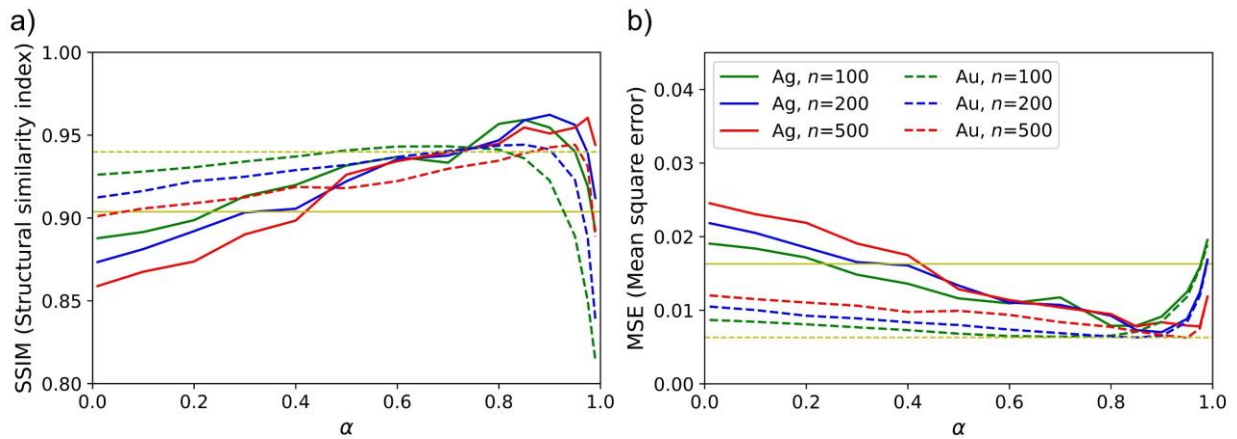


Figure 13 Variation of a) SSIM and b) MSE as a function of α for different n : 100 (green), 200 (blue), and 500 (red) for the quantitative elemental maps obtained using HEBT. Solid lines represent the data for Ag, and dashed lines represent the data for Au. The yellow horizontal lines indicate the best image quality obtained using the EDS-STEM tomographic reconstruction.

The variations of SSIM and MSE as a function of α for the quantitative elemental maps are presented in Figure 13 for different n . The yellow horizontal lines correspond to the best image quality obtained from the quantification of the EDS-STEM tomographic reconstruction (solid line for Ag and dashed line for Au). The quality of the Ag elemental map is greatly improved by the well-determined object boundary. However, the quality of the Au elemental map is at a comparable

level with the Au map before quantification. The different effect on Ag and Au is intrinsic, i.e., because the particle contains higher Ag content in the shell (80 wt%) and it therefore should demonstrate a higher contrast in the quantified composition map. The slight unusual fluctuation of the two metrics with α results from the threshold determination to define the particle volume, because this was done independently via the ESF method each time.

3.2. A particle of flux melted metal-organic framework glass

The two reconstruction techniques and quantification processes were next applied to 3D characterisation of a real experimental dataset obtained from a multicomponent zeolitic imidazolate framework (ZIF) glass: the a_g [(ZIF-67)_{0.2}(ZIF-62)_{0.8}] flux melted glass.

3.2.1. Specimen and experimental data

ZIFs, a subcategory of metal-organic framework, are composed of tetrahedral metal nodes connected by imidazolate-based organic ligands [39]. a_g [(ZIF-67)_{0.2}(ZIF-62)_{0.8}] is generated through the melting of ZIF-67 [Co(mlm)₂, mlm: 2-methylimidazolate, C₄H₅N₂⁻] mixed with ZIF-62 [Zn(lm)_{1.75}(blm)_{0.25}, lm: imidazolate, C₃H₃N₂⁻, and blm: benzimidazolate, C₇H₅N₂⁻] and brought to above the melting point of ZIF-62 [20]. The subscripts, 0.2 and 0.8, refer to the weight fraction of each component, and a_g refers to melt quenched glass. For additional details of the synthesis and previous EDS tomography analysis of this sample, refer to [20] and [21], respectively.

The experimental maps were acquired on a Thermo Fisher 80-200 keV probe corrected Titan with a four quadrant Super-X EDS detector operating at 80 keV. The EDS spectrum image data sets were acquired for different tilt angles ranging from -72° to 54° with a tilt increment of around 9°. For each tilt angle, an ADF image was simultaneously obtained using a Fischione HAADF detector. ADF images have been proved to satisfy the projection requirement, that the signal is a monotonic function of the thickness, in a prior report [21]. It is, therefore, reasonable to use this signal in conjunction with EDS for a HEBT reconstruction. Please refer to reference [21] for more details about the experimental setup.

EDS maps were recorded with a pixel size approximately equal to the beam diameter, and then subsequently re-binned to make sure that each pixel contains enough X-ray counts. Both the EDS spectrum images and ADF images (required to have the same size as EDS maps) were re-binned

to half of their original number of pixels in both spatial dimensions. The pixel size after re-binning is 2.74×2.74 nm. For the acquired EDS spectra, the background was subtracted, and the intensities of the peak of the C, N, Co, and Zn $K\alpha$ line were integrated respectively to generate EDS maps using HyperSpy [40], an open source Python library. The ADF images and EDS maps for the same tilt angle were aligned by aligning the center of mass of ADF image with the elemental map of N. To reduce the shadowing effect, the total signals of a tilt series EDS maps for a certain element were normalized to the same value [41]. The in-plane alignment and tilt-axis shift and rotation were then performed for both ADF and EDS images. Figure 14 shows the processed ADF and EDS images of the C, N, Co and Zn $K\alpha$ line for tilt angles: -45° , 0° , and 45° .

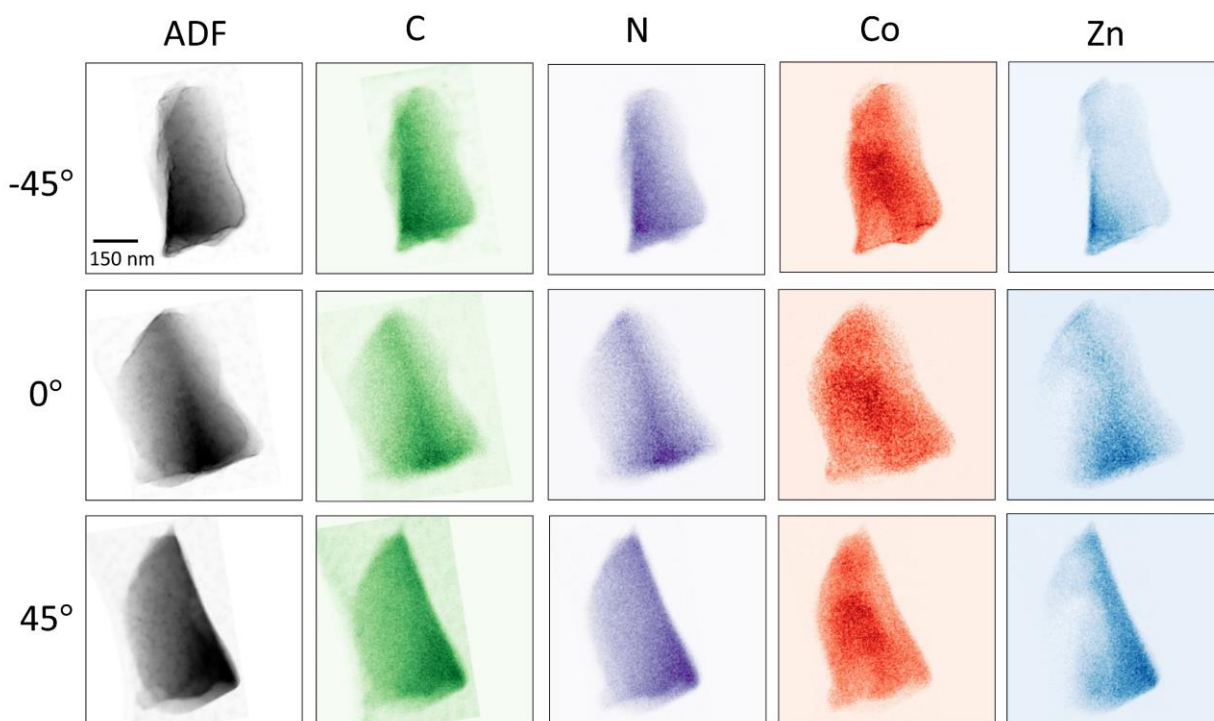


Figure 14 ADF and EDS maps for the C, N, Co, and Zn $K\alpha$ line for tilt angles of -45° , 0° , and 45° . Note the presence of the carbon support film is visible in both the ADF maps and the EDS maps for the C $K\alpha$ line, and the ADF maps are presented here on an inverted intensity scale.

3.2.2. Tomographic reconstruction

Since the weight fraction of H is relatively small for both components (4.6 wt% in ZIF-67 and 3.1 wt% in ZIF-62), the contribution of H to the elastic scattering of electrons, i.e., HAADF signals is ignored. Therefore, only four elements: C, N, Co, and Zn are considered for the HEBT reconstruction.

The HEBT reconstructions were performed for around 260 slices with $\alpha = 0.8$ and $n = 100$. The computed response factors for the four elements are $r_C = 1921$, $r_N = 3792$, $r_{Co} = 5179$, and $r_{Zn} = 6502$ with a coefficient of determination $R^2 = 0.92$. The reconstructed elemental maps are compared with the results from the EDS-STEM tomographic reconstruction in Figure 15, which presents the 2D reconstructed images for slice number 70, 130, and 190.

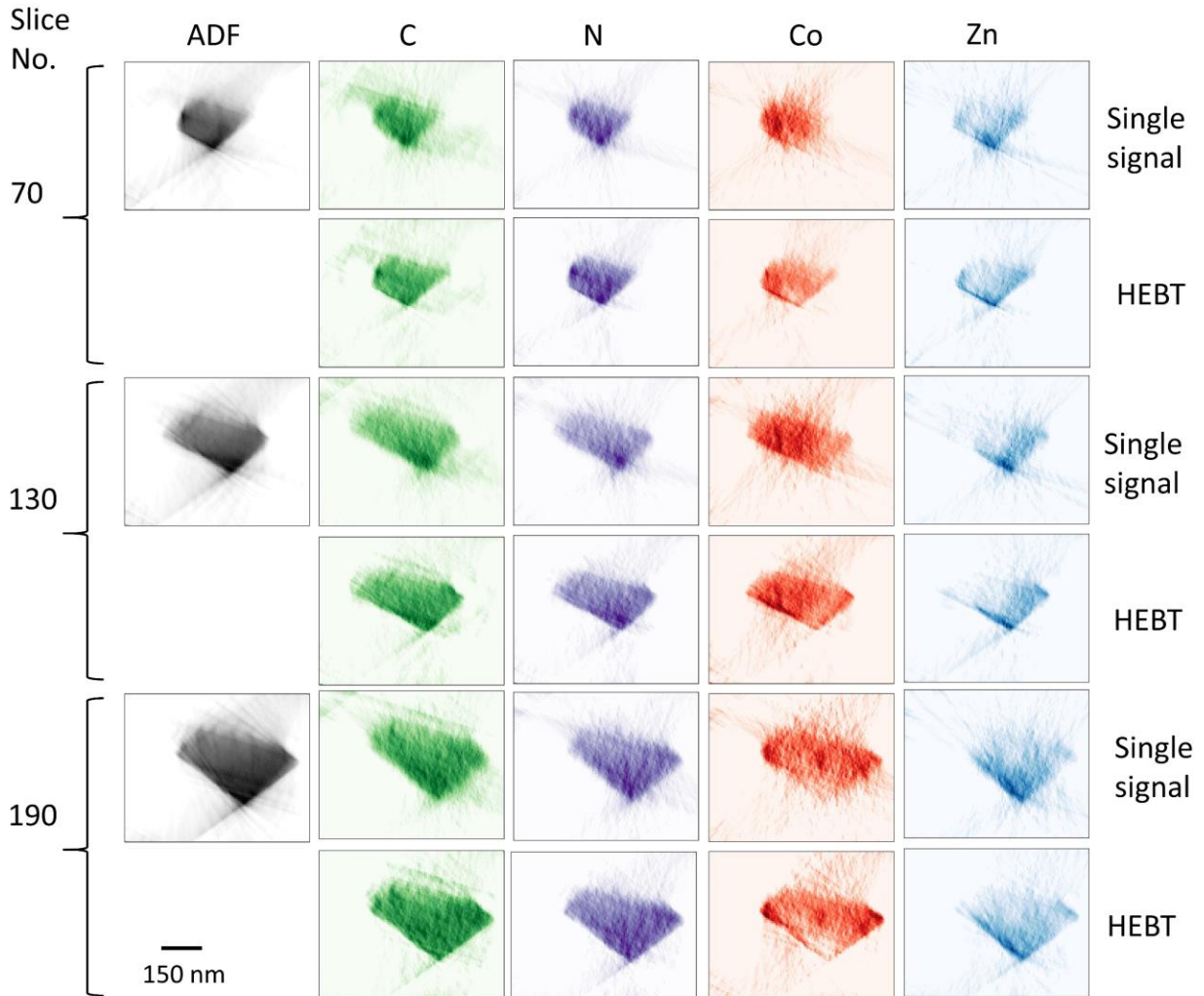


Figure 15 Reconstructed elemental maps for xz orthoslice (the cross-section view in/out of the paper for the maps shown in Figure 14) using the traditional single signal tomography reconstruction and HEBT reconstruction for three slices: no. 70, 130, and 190.

For both EDS-STEM tomography and HEBT, no clear boundaries between the Zn-rich and Co-rich components is observed. Instead, the interface displays the diffusion of the two components resulting in a region comprised of both Co and Zn, consistent with what has been presented in prior reports [20, 21]. Moreover, a higher intensity of Co and little intensity of Zn are

shown in the upper-left region of the particle, likely referring to remnant pure single-phase ZIF-67. Meanwhile the bottom of the particle, displaying high Zn intensity and an apparent absence of Co, likely contains a region corresponding to pure ZIF-62 domain. As we increase the slice number from 70 to 190, the cross-sectional area of the particle increases.

Compared with the EDS-STEM tomographic reconstruction, the HEBT reconstruction, in most cases, displays clearer boundaries and a better contrast. For example, for the Co element map at slice no.190, noise shows in the bottom-right region outside the particle for the EDS-STEM tomographic reconstruction, while it is mostly absent in the reconstructed map from HEBT, making the blurry boundary between the particle and the background much sharper.

Some slight discrepancies in the shape of the particle between the two reconstruction techniques are observed. For example, for slice no.70, a “stripe-like” region along the bottom-right side in the HEBT reconstruction is missing in the elemental maps of the EDS-STEM tomographic reconstruction. This might be due to the misalignment between the ADF images and EDS maps considering that ADF images have only one frame, while EDS spectrum images were acquired as a summation over multiple frames with drift correction.

3.2.3. Quantification

The reconstructed images were then quantified using the physical parameters acquired from MC X-ray. Considering that the X-ray intensities of the C and N K α lines extracted from the spectra can be inaccurate because of the poor background simulation at low energies, presence of the carbon support film underneath the particle, and possible enhancement in the absorption effects [21], C and N were not included in the quantification. We use the weight ratios of Zn and Co to the total weight of Zn and Co [$Zn / (Zn + Co)$ and $Co / (Zn + Co)$] to indicate the quantities of Zn and Co, respectively. The HEBT quantification factors for Co and Zn are $z_{Co} = 9.49 \times 10^4 \text{ b} \cdot \text{mol/g}$ and $z_{Zn} = 9.96 \times 10^4 \text{ b} \cdot \text{mol/g}$. And the EDS-STEM quantification factors are $f_{Co} = 2.25 \text{ b} \cdot \text{mol/g}$ and $f_{Zn} = 1.84 \text{ b} \cdot \text{mol/g}$. According to the definitions of the partial cross-section σ_{par}^A and the EDS quantification factor f_A , we have $\sigma_{par}^{Co} / \sigma_{par}^{Zn} = (f_{Co} \cdot M_{Co}) / (f_{Zn} \cdot M_{Zn})$. In comparison to the partial cross-section ratio of $\sigma_{par}^{Co} / \sigma_{par}^{Zn} = 1.08$, determined experimentally by Collins et al. [21], our calculation obtains a close value of $(f_{Co} \cdot M_{Co}) / (f_{Zn} \cdot M_{Zn})$, 1.10, which indicates the reliability of our model.

Figure 16 presents the absolute weight fraction of Co and Zn for three slices using the two different reconstruction techniques. Similar features as observed in Figure 15 are shown in Figure 16, that high Co concentration is found in the upper-left region, and high Zn concentration in the bottom-right region. Even though the same threshold determination method was used, the HEBT reconstruction shows smoother boundaries and a more similar shape to the reconstructed images before quantification as observed in Figure 15 than the EDS-STEM tomographic reconstruction. Again, small discrepancies in the shape might result from the misalignment between the ADF images and EDS maps.

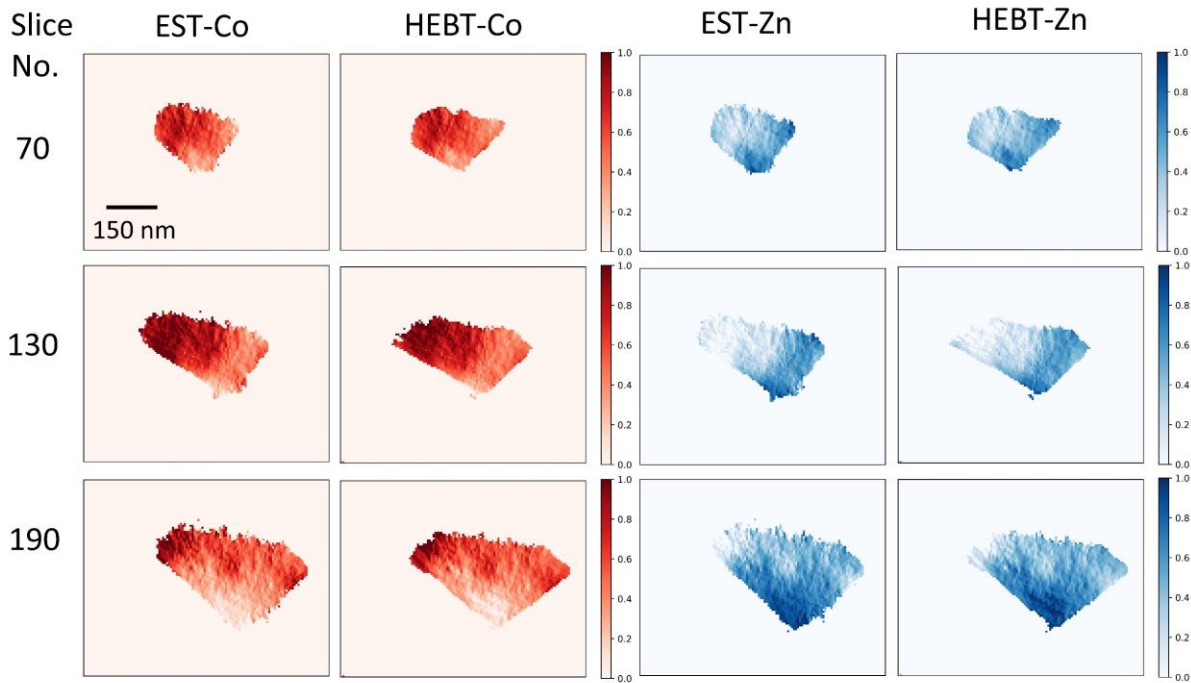


Figure 16 Weight fraction maps of Co and Zn [$Co/(Co + Zn)$ and $Zn/(Co + Zn)$] using the EDS-STEM tomographic and HEBT reconstruction for slice no. 70, 130, and 190 (cross-section view on the xz plane).

Figure 17 presents a 3D volume rendering of the flux melted particle obtained using the quantification of the HEBT reconstruction, which provides a complete view to observe the 3D morphology and diffusion of the Co-rich domain (red) and Zn-rich domain (blue) in the particle.

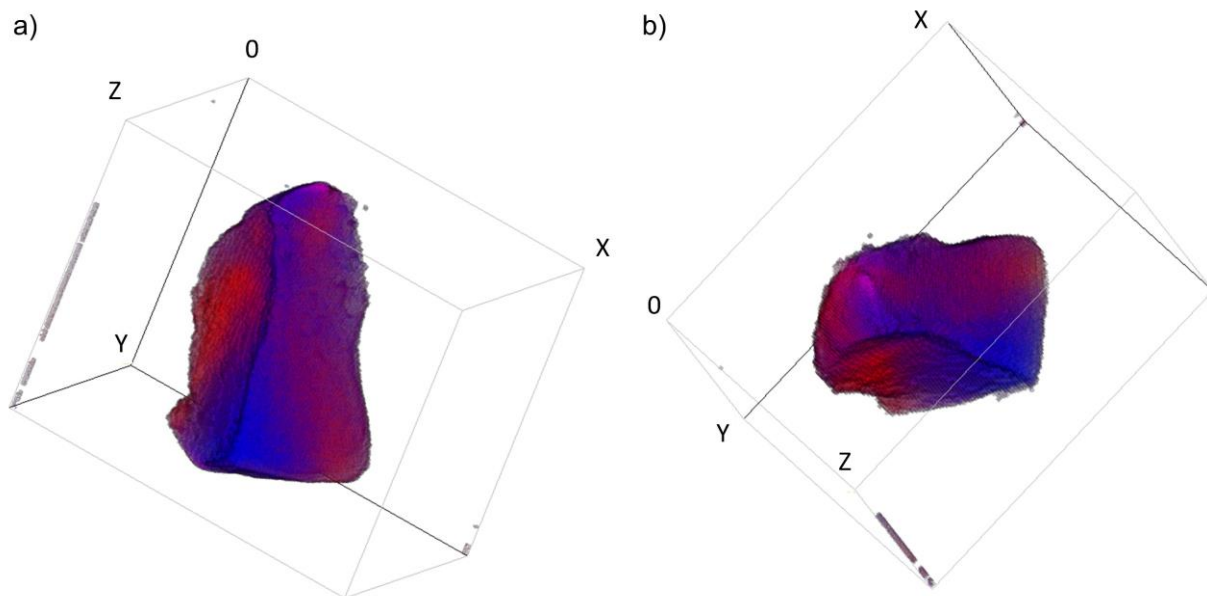


Figure 17 3D volume rendering of the flux melted particle using the HEBT reconstruction. Red represents Co, and blue represents Zn.

4. Conclusion

We have proposed a new quantification approach combining the physical parameters acquired from MC X-ray with tomographic reconstruction to characterize 3D elemental distribution of nanostructures quantitatively. Two types of tomographic reconstruction were investigated using the simultaneous iterative reconstruction technique (SIRT): the traditional EDS-STEM tomographic reconstruction and HAADF-EDS bimodal tomographic (HEBT) reconstruction. The two types of reconstruction technique and the corresponding quantification approaches were applied to a simulated dataset of a 2D phantom sample of a Ag-Au nanoparticle and an experimental dataset of a particle of flux melted metal-organic framework glass.

Using the simulated dataset of a 2D phantom sample (a single slice), the effects of the reconstruction parameters were investigated through two type of image quality metrics: SSIM and MSE. For both EDS-STEM tomography and HEBT, the quality of the reconstructed image is initially improved as a function of the number of iterations, before falling off at higher values due to the over-fitting problem. A similar trend was observed for α , the weight of the HAADF signal, in the HEBT reconstruction. Moreover, as α increases, the approximately optimal value for the number of iterations increases since the optimization becomes less efficient as α increases. In general, with appropriate reconstruction parameters, HEBT shows a better contrast and a reduced

noise level compared with EDS-STEM tomography. The quantified elemental maps obtained from the HEBT reconstruction also present a better similarity and lower errors in comparison to the reference images when compared to that from the EDS-STEM tomographic reconstruction.

The quantification approaches of both reconstruction techniques were successfully applied to an experimental dataset of a particle of flux melted metal-organic framework glass, displaying the quantified 3D elemental distribution of Co and Zn. The diffusion of the Co-rich domain and Zn-rich domain into each other was shown. The EDS-STEM tomography quantification factors calculated using our approach have shown a good consistency with the experimentally measured partial cross-sections from the reference.

We have shown the feasibility of our quantification approaches for EDS-STEM tomography and HEBT applied to experimental datasets. Using SIRT, both EDS-STEM tomography and HEBT have revealed physically meaningful results. Although requiring an optimal alignment of ADF and EDS maps in conventional multi-frame acquisitions, HEBT has shown advantages in image contrast, boundary determination, and noise reduction compared with EDS-STEM tomography. The HEBT technique will play an important role in the characterization of beam-sensitive samples for which the EDS maps are quite noisy and in reducing experimental acquisition time. In the future, the method to better align the ADF and EDS maps will be explored. And the integration of other advanced tomography algorithms as a replacement of SIRT will be implemented to improve the reconstructed images.

Acknowledgement

Y. Y. acknowledges financial support from Natural Sciences and Engineering Research Council of Canada (NSERC). K. E. M. acknowledges the Deutsche Forschungsgemeinschaft (DFG) for funding this research through Grant HE 7192/1-2. S. M. C. acknowledges support from a University Academic Fellowship at the University of Leeds.

References

1. Pennycook, S.J. and P.D. Nellist, *Scanning transmission electron microscopy: imaging and analysis*. 2011: Springer Science & Business Media.
2. Lučić, V., F. Förster, and W. Baumeister, *Structural studies by electron tomography: from cells to molecules*. *Annu. Rev. Biochem.*, 2005. **74**: p. 833-865.

3. Bárcena, M. and A.J. Koster. *Electron tomography in life science*. in *Seminars in cell & developmental biology*. 2009. Elsevier.
4. Weyland, M. and P.A. Midgley, *Electron tomography*. *Materials Today*, 2004. **7**(12): p. 32-40.
5. Pennycook, S., *Z-contrast STEM for materials science*. *Ultramicroscopy*, 1989. **30**(1-2): p. 58-69.
6. Goris, B., et al., *Monitoring galvanic replacement through three-dimensional morphological and chemical mapping*. *Nano Lett*, 2014. **14**(6): p. 3220-6.
7. Rossouw, D., et al., *Blind source separation aided characterization of the γ' strengthening phase in an advanced nickel-based superalloy by spectroscopic 4D electron microscopy*. *Acta Materialia*, 2016. **107**: p. 229-238.
8. Rueda-Fonseca, P., et al., *Quantitative reconstructions of 3D chemical nanostructures in nanowires*. *Nano letters*, 2016. **16**(3): p. 1637-1642.
9. Slater, T.J., et al., *STEM-EDX tomography of bimetallic nanoparticles: A methodological investigation*. *Ultramicroscopy*, 2016. **162**: p. 61-73.
10. MacArthur, K.E., et al., *Quantitative energy-dispersive X-ray analysis of catalyst nanoparticles using a partial cross section approach*. *Microscopy and Microanalysis*, 2016. **22**(1): p. 71-81.
11. Saghi, Z., et al., *Three-dimensional chemical analysis of tungsten probes by energy dispersive x-ray nanotomography*. *Applied Physics Letters*, 2007. **91**(25): p. 251906.
12. Burdet, P., et al., *A novel 3D absorption correction method for quantitative EDX-STEM tomography*. *Ultramicroscopy*, 2016. **160**: p. 118-129.
13. Zanaga, D., et al., *A new method for quantitative XEDS tomography of complex heteronanostructures*. *Particle & Particle Systems Characterization*, 2016. **33**(7): p. 396-403.
14. Zhong, Z., et al., *A bimodal tomographic reconstruction technique combining EDS-STEM and HAADF-STEM*. *Ultramicroscopy*, 2017. **174**: p. 35-45.
15. Bender, H., et al., *Combined STEM-EDS tomography of nanowire structures*. *Semiconductor Science and Technology*, 2019.
16. Cliff, G. and G.W. Lorimer, *The quantitative analysis of thin specimens*. *Journal of Microscopy*, 1975. **103**(2): p. 203-207.
17. Watanabe, M. and D. Williams, *The quantitative analysis of thin specimens: a review of progress from the Cliff-Lorimer to the new ζ -factor methods*. *Journal of microscopy*, 2006. **221**(2): p. 89-109.
18. Watanabe, M., D.B. Williams, and Y. Tomokiyo, *Comparison of detectability limits for elemental mapping by EF-TEM and STEM-XEDS*. *Micron*, 2003. **34**(3-5): p. 173-183.
19. MacArthur, K., et al., *Compositional quantification of PtCo acid-leached fuel cell catalysts using EDX partial cross sections*. *Materials Science and Technology*, 2016. **32**(3): p. 248-253.
20. Longley, L., et al., *Flux melting of metal-organic frameworks*. *Chemical Science*, 2019. **10**(12): p. 3592-3601.
21. Collins, S.M., et al., *Phase diagrams of liquid-phase mixing in multi-component metal-organic framework glasses constructed by quantitative elemental nano-tomography*. *APL Materials*, 2019. **7**(9): p. 091111.

22. Gauvin, R. and P. Michaud, *MC X-Ray, a new Monte Carlo program for quantitative X-ray microanalysis of real materials*. *Microscopy and Microanalysis*, 2009. **15**(S2): p. 488-489.
23. Armigliato, A., *X-ray Microanalysis in the Analytical Electron Microscope*. 1992, Singapore, World Scientific. p. 431-456.
24. Kak, A. and M. Slaney, *Principles of computerized tomographic imaging IEEE Press*. New York, 1988.
25. Gregor, J. and T. Benson, *Computational analysis and improvement of SIRT*. *IEEE transactions on medical imaging*, 2008. **27**(7): p. 918-924.
26. Gilbert, P., *Iterative methods for the three-dimensional reconstruction of an object from projections*. *Journal of theoretical biology*, 1972. **36**(1): p. 105-117.
27. Leary, R.K. and P.A. Midgley, *Electron Tomography in Materials Science*, in *Springer Handbook of Microscopy*. 2019, Springer. p. 2-2.
28. Nikazad, T. and M. Karimpour, *Controlling semi-convergence phenomenon in non-stationary simultaneous iterative methods*. *Iranian Journal of Numerical Analysis and Optimization*, 2016. **6**(2): p. 51-64.
29. Hansen, P.C. and M. Saxild-Hansen, *AIR tools—a MATLAB package of algebraic iterative reconstruction methods*. *Journal of Computational and Applied Mathematics*, 2012. **236**(8): p. 2167-2178.
30. Hawkes, P., *Electron Tomography: 3D imaging in the TEM*. 1992, New York: Plenum.
31. Zhong, Z., et al., *Numerical methods for low-dose EDS tomography*. *Ultramicroscopy*, 2018. **194**: p. 133-142.
32. Browning, R., *Universal elastic scattering cross sections for electrons in the range 1–100 keV*. *Applied physics letters*, 1991. **58**(24): p. 2845-2847.
33. Bote, D., et al., *Cross sections for ionization of K, L and M shells of atoms by impact of electrons and positrons with energies up to 1 GeV: Analytical formulas*. *Atomic Data and Nuclear Data Tables*, 2009. **95**(6): p. 871-909.
34. Perkins, S., et al., *Tables and graphs of atomic subshell and relaxation data derived from the LLNL Evaluated Atomic Data Library (EADL), Z= 1--100*. 1991, Lawrence Livermore National Lab., CA (United States).
35. Hasinoff, S.W., *Photon, Poisson Noise*. 2014.
36. Virtanen, P., et al., *SciPy 1.0: fundamental algorithms for scientific computing in Python*. *Nature methods*, 2020. **17**(3): p. 261-272.
37. Wang, Z., et al., *Image quality assessment: from error visibility to structural similarity*. *IEEE transactions on image processing*, 2004. **13**(4): p. 600-612.
38. Ruder, S., *An overview of gradient descent optimization algorithms*. arXiv preprint arXiv:1609.04747, 2016.
39. Park, K.S., et al., *Exceptional chemical and thermal stability of zeolitic imidazolate frameworks*. *Proceedings of the National Academy of Sciences*, 2006. **103**(27): p. 10186-10191.
40. de la Peña, F., et al., *HyperSpy 1.3*. 2017, Hyperspy.
41. Slater, T., et al. *Understanding the limitations of the Super-X energy dispersive X-ray spectrometer as a function of specimen tilt angle for tomographic data acquisition in the S/TEM*. in *Journal of Physics: Conference Series*. 2014. IOP Publishing.